Interface engineering of graphene nanosheet reinforced ZrB$_2$ composites by tuning surface contacts

Yanhui Zhang[*] and Stefano Sanvito[†]

School of Physics and CRANN, Trinity College, Dublin 2, Dublin, Ireland

The mechanical properties of heterophase interfaces are critically important for the behavior of graphene-reinforced composites. In this work, the structure, adhesion, cleavage, and sliding of heterophase interfaces formed between a ZrB$_2$ matrix and graphene nanosheets are systematically investigated by density functional theory and compared to available experimental data. We demonstrate that the surface chemistry of the ZrB$_2$ matrix material largely shapes the interface structures and the nature of the interfacial interaction. Zr-C interfaces present strong chemical bonding and their response to mechanical stress is significantly influenced by graphene corrugation. In contrast B-C interfaces, interacting through relatively weak π-π stacking, show attributes similar to those of two-dimensional materials heterostructures. Our theoretical results provide insights into the interface bonding mechanisms in graphene/ceramic composites, and highlight the prospects for their design via interface engineering enabled by surface contacts.

I. INTRODUCTION

In the last ten years the use of graphene as nanofiller in ceramic matrix composites (CMCs), the so called graphene-reinforced CMC (GCMC) materials, has attracted plenty of research interest. GCMCs find application in various industry sectors such as aerospace, automotive, energy and power, micro-electronics, and pharmaceutical [1–4]. In addition to the excellent electronic, thermal, and mechanical properties (a tensile strength of 130 GPa and a Young's modulus of 1 TPa), the extremely high specific surface area of graphene (2630 m^2 g^{-1}) provides great capacity for the modification and the functionalization of ceramic composites [5,6]. For instance, the fracture toughness parameter K_{IC} of Si$_3$N$_4$ can be improved by as much as 235% by adding 1.5 vol % of graphene [4]. Toughness improvements are also found for zirconium diboride (ZrB$_2$) [7–9], silicon carbide (SiC) [10], tantalum carbide (TaC$_x$) [11], and alumina (Al$_2$O$_3$) [12]. At the same time, the addition of graphene to a ceramic matrix can also suppress the growth of unwanted oxide layers and refine the grain structure [7,13]. Last but not least, the mechanical and functional properties of GCMCs can be simultaneously improved by developing hierarchical architectures [8,14,15].

Among the various ceramic materials that can benefit from graphene-based nanofillers, ZrB$_2$, classified as an ultrahigh temperature ceramic (UHTC), is one of the most promising structural compounds for aerospace propulsion and thermal protection systems [16,17]. ZrB$_2$ exhibits a unique combination of high melting point ($T_m \sim 3246\,°C$), chemical inertness, effective wear, and resistance to the environment. However, the relatively weak fracture toughness and both the drop of flexural strength and the limited oxidation resistance at high temperature [18] are drawbacks awaiting for solutions. Adding to a ZrB$_2$ matrix continuous fibers for enhancing the fractural toughness and the flexural strength [19], and nanoparticles, such as SiC, for improving the oxidation resistance [20] can partially overcome these issues. Very recently, the incorporation of graphene into a ZrB$_2$ matrix [7–9] has risen expectations for the formation of ZrB$_2$/graphene composites with enhanced structural and mechanical stability, in particular at high temperature. Most of the properties of such composites depend strongly on the behavior of the various interfaces forming between uneven materials, which determine the debonding behavior and the fracture toughness in the resulting GCMCs.

A satisfactory identification of the most abundant interface types in GCMCs is not an easy task and so is the assignment of specific mechanical properties to each type. Experimentally the difficulties are related to the nanosized scale and morphology of the fillers, to the presence and variation of defects along the interfaces, and to the sophisticated details of the interface alignments. Since such interfaces are typically buried in the material, atomic-resolved microscopy is usually difficult to perform. Additional complexity originates from the data deconvolution needed to fit the experimentally measured quantities to physical models [21–23]. In general, however, one expects a large variation of interface types and structures, since most of the GCMC materials are manufactured with highly nonequilibrium methods, such as spark-plasma sintering, which are affected by skin effects and the large temperature gradients [24]. As a result not only thermodynamically stable interfaces form, but also metastable and possible unstable ones.

A valid alternative and complement to extensive experimental studies is offered by atomistic simulations, in particular by molecular dynamics (MD) [25–27]. MD can be used to investigate the bonding energy and the stability of interfaces and, in principle, it enables one to establish a one-to-one

---
[*]yzhang1@tcd.ie
[†]sanvitos@tcd.ie

correlation between the microscopic structure and the mechanical properties of an interface at different temperatures. Also in this case, however, there are some drawbacks. On the one hand, when the MD is performed with classical force fields [27] the accuracy may be an issue. This is particularly problematic when the interfaces may include very different bonding types, as we will show here for ZrB_2/graphene. On the other hand, *ab initio* MD based on density functional theory (DFT) is highly accurate but computationally expensive. As a consequence it becomes impractical when many different interface types are relevant. A good compromise may be offered by extensive *ab initio* total-energy studies for large supercells containing interfaces [28–30]. Such an approach is followed here for the investigation of ZrB_2/graphene. In particular, since we do not have any previous knowledge of the interfacial structure in actual samples, we construct a wide range of interface types and morphologies. These are obtained by combining the most thermodynamically stable ZrB_2 surfaces with graphene, a situation likely to occur during the spark-plasma sintering process.

The paper is organized as follows. First, we discuss the possible atomistic interfacial models and introduce their notation (Sec. III A). Then, in Sec. III B, the interfacial adhesion and binding strength are analyzed for the various interfaces. Different interfacial structural variables, such as the type of surface contacts, the interfacial strain, and the stacking sequence are considered. Next, the interfacial strength is investigated with respect to two kinds of fracture deformation modes: (i) opening/tensile mode (Sec. III C) and (ii) sliding or in-plane shear mode (Sec. III D). Thereafter, the microscopic/electronic mechanism for the interfacial bonding of the Zr-C and B-C surface contacts are presented in Sec. III E. In the final discussion section we critically review our work by addressing the possibility of engineering the mechanical properties of ZrB_2/graphene composites by controlling the abundance of the various ZrB_2 surfaces available to form surface contacts. This provides guidelines to future experimental work on GCMC materials.

Our work ultimately demonstrates that the interfacial strengths of graphene-reinforced ZrB_2 nanocomposites can be largely engineered by an appropriate choice of surfaces, with variations up to an order of magnitude. This is because the interfacial bonding mechanism may vary from a covalent bond at the Zr-C interfaces to a π-π stacking type at the B-C ones, with corrugation playing an important role. Thus, the engineering of the interfacial properties of graphene/ZrB_2 nanocomposites is achievable by tuning the ZrB_2 growth chemical environment, which leads to a rich variety of Zr-, B- and mix-terminated surfaces.

II. METHODOLOGY

First-principles calculations are performed within the DFT framework by using the plane-wave basis projector augmented wave method [31] as implemented in the VASP code [32]. The generalized gradient approximation (GGA) parametrized by Perdew, Burke, and Ernzerhof (PBE) [33] provides the exchange-correlation energy and potential. In addition, damped van der Waals corrections (DFT-D2) [34] are included to account for long-range dispersion interactions. The reliability of the PBE+D2 method in describing transition metal diborides and graphite has been established before [35,36].

The Brillouin zone of the supercells describing our interface models are sampled by using the Monkhorst-Pack k-point method, with the following k meshes, $16\times16\times1$, $14\times14\times1$, and $12 \times 7 \times 1$, respectively for interface supercells I, II, and III (the structural details of these interface models will be introduced in Sec. III A). The plane-wave kinetic energy cutoff is set to 500 eV. These parameters have all been tested to ensure an energy convergence of 1 meV/atom.

III. RESULTS

A. Interface configurations

Our working hypothesis in constructing the various interface models is that heterophase interfaces form during sintering by creating a mechanical contact between the ZrB_2 matrix and the graphene nanosheets. Thus, the most probable interfaces involve the most thermodynamically stable ZrB_2 surfaces, namely the Zr- and B-terminated (0001) and the Zr-terminated (10$\bar{1}$0) ones. Such attribution has been suggested by previous DFT calculations [35] and have been validated by experiments [37,38]. We then construct 12 interface models by sandwiching graphene between two stable ZrB_2 surfaces, namely by simulating ZrB_2/graphene/ZrB_2 trilayers as schematically shown in Fig. 1(a). Potentially also the $(11\bar{2}2)_{Zr+B}$ surface, with mixed Zr and B termination, and the $(11\bar{2}3)_{Zr}$ one are stable under specific growth conditions [35]. These are not considered here, as we only focus on the two extreme cases of purely Zr- and B-terminated surfaces. However, such richness in the possible surface termination as a function of the chemical environment at growth, suggests that one can effectively tune the likely surface-type abundance of the matrix to expose to the sintering process.

We consider only commensurate interface models, in which the ZrB_2 slab and the graphene monolayer are constrained to have a common lateral lattice parameter. Misfit dislocations are not explicitly investigated since they require extremely large supercells, which are beyond the standard DFT capability. The thicknesses of the various interfaces are set between 17 and 26 atomic layers (see the thickness test in the Supplementary Information (SI) of Ref. [35]). The two far ends of such hybrid structures are separated by a vacuum region of 16 Å in order to prevent the artificial interaction between the periodic replicas. It is known that the Zr-terminated surfaces have low surface strains [35]. Therefore, the two ZrB_2 surfaces facing the vacuum regions are all Zr terminated so to reduce the possible effects arising from surface dipoles and ruffling.

By using the coincidence lattice method [39], graphene and ZrB_2 slabs are joined to form interface junctions. In a nutshell the method consists of rotating and straining the graphene and ZrB_2 lattices so to obtain one supercell with common lattice vectors and small lattice mismatch that, at the same time, contains a reasonable number of atoms. Such exercise has returned us three optimum supercells, where the ZrB_2 slabs have the following superstructures: (I) $\sqrt{3} \times \sqrt{3}$ (0001), (II) 2×2 (0001), and (III) 2×3 (10$\bar{1}$0). These define three different interface supercells, labeled as I, II, and III
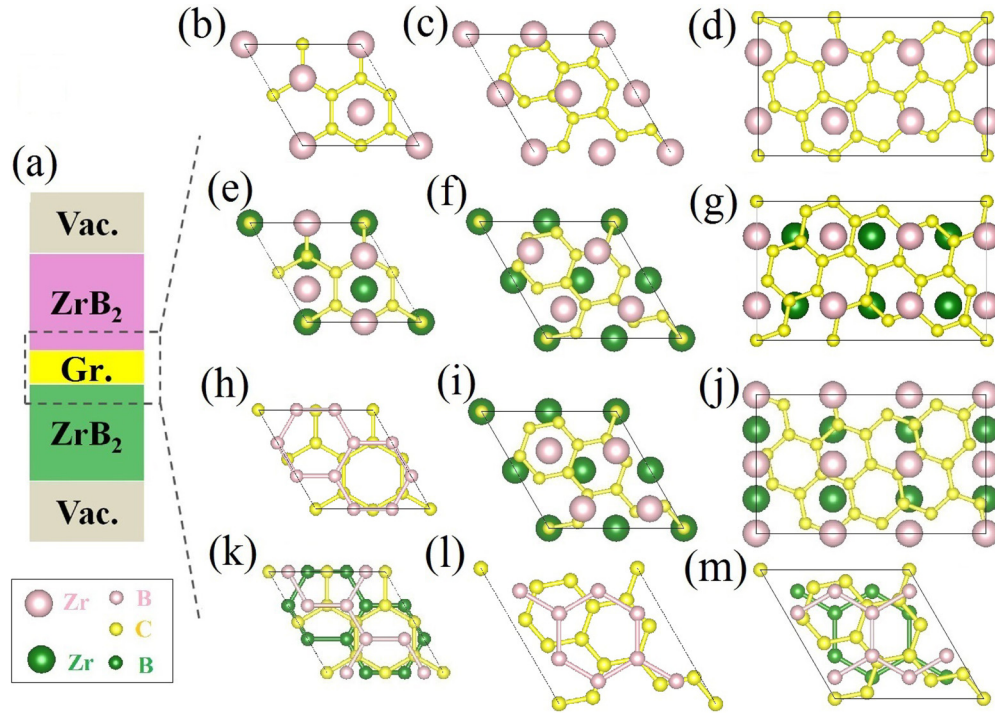
FIG. 1. Summary of the interface supercells constructed in this work. (a) A schematic drawing of the trilayer structure used in our simulations. The top view of the interface regions enclosed in the dashed box are illustrated in (b) through (m): (b) I_{Zr-C}^{AA}, (c) II_{Zr-C}^{AA}, (d) III_{Zr-C}^{AA}, (e) I_{Zr-C}^{AB}, (f) II_{Zr-C}^{AB}, (g) III_{Zr-C}^{AB}, (h) I_{B-C}^{AA}, (i) II_{Zr-C}^{AC}, (j) $III_{Zr-C}^{AB'}$, (k) I_{B-C}^{AB}, (l) II_{B-C}^{AA}, and (m) II_{B-C}^{AB}. Atoms belonging to the top (bottom) ZrB$_2$ slabs are colored in pink (green), while those of graphene (Gr) are in yellow. Large spheres indicate Zr and small ones B. See the main text for the convention used to define the various interfaces. Note that the models in (g) and (j) are both AB type, but present an inequivalent atomic arrangement.

[see Figs. 1(b)–1(d)], with a lattice mismatch of $\Delta a = 10\%$, $\Delta a = 2\%$, and $\Delta a = 3\%$ ($\Delta b = 6\%$), respectively (a and b are the in-plane lattice parameters of the interface supercells). A second characteristic defining the interfaces is the stacking order at the ZrB$_2$ ends. We denote as AA the situation where the two ZrB$_2$ slabs neighboring the graphene layer are symmetric, so that the Zr atoms of the upper slab are on top of the same kind of atoms in the lower slab [see Figs. 1(b), 1(c), 1(d), 1(h), and 1(l)]. In contrast, the stacking is called AB type when the Zr atoms of the top ZrB$_2$ slab are in a bridge position with respect to those at the bottom [see Figs. 1(e), 1(f), 1(g), 1(j), 1(k), and 1(m)]. Finally AC stacking denotes the situation where the atoms in top ZrB$_2$ slab occupy the hollow positions [see Fig. 1(i)].

Taking all this into consideration each hybrid structure is uniquely defined by (1) the supercell type, (2) the stacking sequence, and (3) the atomic species of the ZrB$_2$ matrix at the interface. For example, II_{Zr-C}^{AA}, II_{Zr-C}^{AB}, and II_{Zr-C}^{AC} describe the interface models having a type II supercell, Zr-C facing species and the stacking sequences AA, AB, and AC, respectively. The top view of the interface regions of these three structures are illustrated in Figs. 1(c), 1(f) and 1(i), which contains the same plots for all the interfaces investigated.

Finally, the ZrB$_2$/graphene interlayer distance d_i, and the common lattice parameters a_i and b_i, are optimized by searching for the lowest energy points of the $E(a_i, b_i, d_i)$ potential energy surface (see Sec. III B 1). The so-calculated parameters are tabulated in Table II in the Appendix, together with the in-plane strains and the characters of various interface models.

At such optimized lattice parameters the ionic positions are fully relaxed into their ground state by using the quasi-Newton algorithm to relieve the residual stresses.

B. Interface binding

The various interface models are first characterized by computing the adhesion energy E_{ad} and the binding energy E_b. Both these quantities are closely related to the interfacial strength, so that they can be used as first indicators before simulating the mechanical behavior in detail. Furthermore, the misfit strain energies U_i for all interfaces are also calculated. Note that U_i measures the elastic energy stored in the interface due to the lattice misfit between graphene and the ZrB$_2$ matrix; E_{ad} provides an essential indicator of the general strength of the surface contact and does include contributions from misfit effects; E_b quantifies the strength of the surface contacts in terms of their pure chemical attachment.

1. Interfacial adhesion energy (E_{ad})

The adhesion energy E_{ad} is defined as the energy per unit area released when forming the trilayered structure from the isolated surface slabs, namely

$$E_{ad} = \frac{E_{tot}(a_i) - E_{top}(a_0) - E_{bot}(a_0) - E_{Gr}(l_{C-C})}{2A}. \quad (1)$$

Here $E_{tot}(a_i)$, $E_{top}(a_0)$, $E_{bot}(a_0)$, and $E_{Gr}(l_{C-C})$ are, respectively, the total DFT energy of the hybrid structure, that of the top and bottom ZrB$_2$ slab, and that of the graphene monolayer. Note that the reference ZrB$_2$ slabs have an in-plane lattice
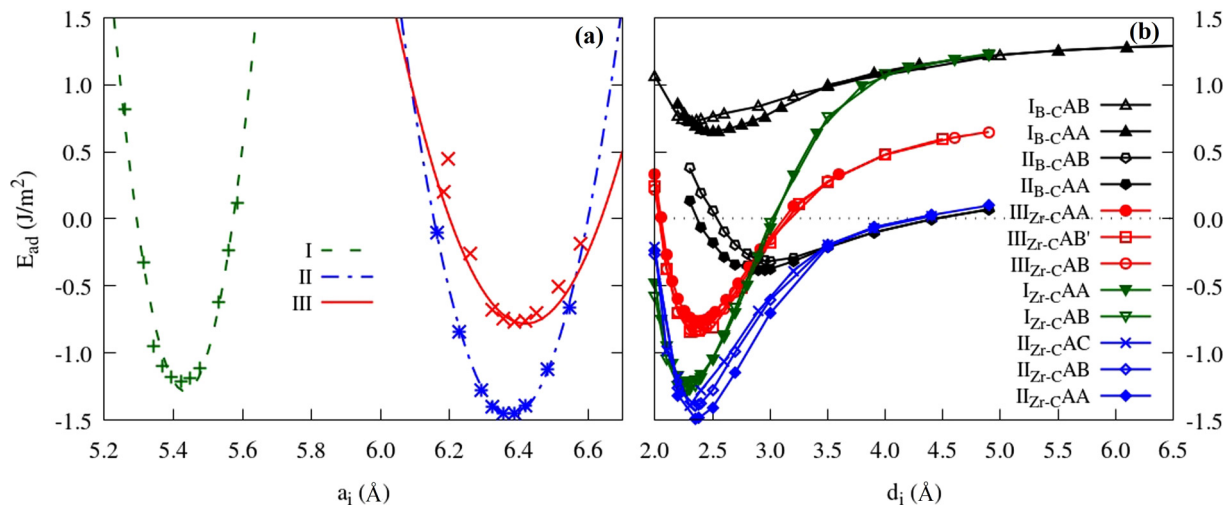
FIG. 2. The variation of the adhesion energy E_{ad} (in J/m^2) as a function of (a) the in-plane lattice parameter a_i (Å), and (b) the interlayer distance d_i (Å). Results are plotted for the three supercell types in (a) at the fixed interlayer distance $d_i = 2.5$ Å. In (b) E_{ad} is computed for all the different interface models introduced in Fig. 1 and the in-plane lattice parameters are fixed to those at the minimum of the corresponding curves in (a).

parameter a_0 corresponding to that of their strain-free surface configuration. Likewise, the reference graphene monolayer has the equilibrium C-C bond length of $l_{C\text{-}C} = 1.42$ Å. As a consequence E_{ad} for the various hybrid structures is computed relatively to the same reference states, namely the strain-free surface slabs. An alternative choice is to take the bulk structures as reference, a choice that will make the surface formation energy included into E_{ad}. Finally, A is the interface area and the prefactor 2 takes into account the fact that our heterostructures have two interfaces.

The calculated $E_{ad}(a_i; d_i)$ curves are presented in Fig. 2(a) for all three kinds of interface supercells I, II, and III, while the interlayer distances d_i are kept fixed at 2.5 Å. A parabolic behavior is observed in all cases, similarly to what recently reported for the interface between graphene and Ti$_2$C MXene [40]. The in-plane lattice parameters of the various interfaces are thus determined from the minima of Fig. 2(a). Then, the optimal interlayer distances d_0 are computed by searching for the minima of the $E_{ad}(d_i; a_i)$ curves, see Fig. 2(b).

Several comments can be made by looking at Fig. 2(b). First, we note that the overall E_{ad} curves move to a lower energy as we go across the series I$_{B\text{-}C}$, II$_{B\text{-}C}$, III$_{Zr\text{-}C}$, I$_{Zr\text{-}C}$, and II$_{Zr\text{-}C}$. Their adhesion strengths therefore have to be ranked in the reverse order. Second, it is quite clear that all the Zr-C interfaces have a $E_{ad}(d_i)$ potential well deeper than those with B-C bonding, suggesting that the Zr-C interfaces are energetically more favorable than the B-C ones. Third, we find that the exact stacking order has little effect on the E_{ad} curves, in particular on their energy minimum, indicating that the local bonding environment plays only a minor role in the interface adhesion. Finally, each E_{ad} curve has a long distance tail that asymptotically converges to a positive E_{ad} value. In particular we have all type I curves converging to $U_{I} = 1.288$ J/m^2, the type II ones to $U_{II} = 0.261$ J/m^2 and

the type III to $U_{III} = 0.838$ J/m^2. Such asymptotic values U_i correspond to the misfit strain energies introduced by imposing a common in-plane lattice parameter. Thus the U_i's are proportional to the misfit strains associated with the setup of the interface models. In fact, the strain energies are ranked in the order $U_{I} > U_{III} > U_{II}$, which is the same order of the in-plane strains.

Although it is too computationally expensive to include misfit dislocations in our DFT calculations, because of the large supercells required, the misfit strain can be effectively released by considering configurations where graphene presents vertical corrugation, an intrinsic feature of graphene flakes on substrates [41]. After full structural relaxation, the Zr-C-Zr structures with AB and AC stacking orders exhibit a more pronounced graphene corrugation than that corresponding to the AA stacking. In contrast, for B-C-B trilayers more pronounced graphene rippling is present for the AA order. The underlying mechanisms leading to these structural differences will be analyzed later when discussing the electronic structure of the interfaces in Sec. III E.

2. Interfacial binding energy

As discussed before, our interface supercells are constructed by using commensurate models so that the heterogeneous layers have common in-plane lattice parameters, a fact that introduces misfit strain. As a consequence, E_{ad} contains contributions originating both from the misfit strain energy U_i and from the chemical/physical interactions at the interface E_b. In order to decouple the two contributions, we assume that E_{ad} can be written as

$$E_{ad} = -E_b + U_i. \qquad (2)$$

The misfit energy U_i can be approximated by the following expression:

$$U_i(a_i) = \frac{[E_{top}(a_i) - E_{top}(a_0)] + [E_{bot}(a_i) - E_{bot}(a_0)] + [E_{Gr}(a_i) - E_{Gr}(l_{C\text{-}C})]}{2A}, \qquad (3)$$
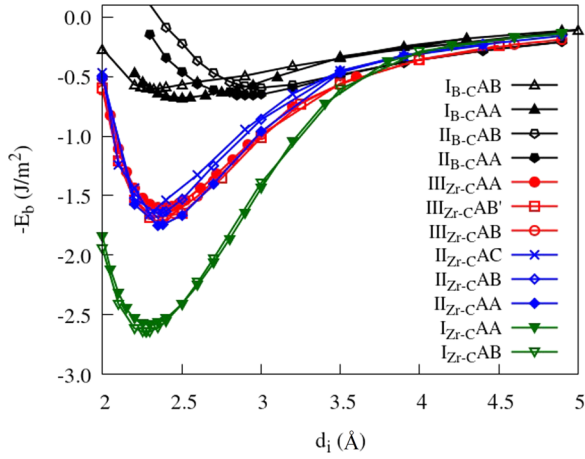
FIG. 3. Interfacial binding energy $-E_b$ (J/m^2) against the interlayer separation distance d_i, (Å).

where $E_{\text{top}}(a_i)$, $E_{\text{bot}}(a_i)$, and $E_{\text{Gr}}(a_i)$ are, respectively, the total energy of the top and bottom ZrB$_2$ slab and that of the graphene monolayer, all taken at the common in-plane lattice parameter a_i. The other terms have been already introduced when discussing Eq. (1). Hence one has

$$-E_{\text{b}}(d_i; a_i) = E_{\text{ad}}(d_i; a_i) - U_i(a_i)$$
$$= \frac{E_{\text{tot}}(d_i; a_i) - E_{\text{top}}(a_i) - E_{\text{bot}}(a_i) - E_{\text{Gr}}(a_i)}{2A}.$$
(4)

The binding energy curves $E_{\text{b}}(d_i; a_i)$ are then presented in Fig. 3. In comparison to $E_{\text{ad}}(d_i)$, as expected, they all asymptotically converge to zero. Interestingly all the $E_{\text{b}}(d_i)$ curves seem to cluster into three main groups: (i) the I$_{\text{Zr-C}}$ interface has the deepest E_{b} well (~ 2.6 J/m^2), indicating strong interfacial interaction; (ii) the interfaces II$_{\text{Zr-C}}$ and III$_{\text{Zr-C}}$ have an intermediate E_{b} minimum at around 1.7 J/m^2, which is 35% lower than that of I$_{\text{Zr-C}}$, suggesting a moderate interfacial interaction; (iii) all the interfaces of B-C type show a very shallow E_{b} profile, with a minimum at around 0.5 J/m^2. This latter value is close to that calculated for graphite (0.4 J/m^2, see discussion section).

It is worthy to mention that E_{ad} and E_{b} for the B-C interfaces are about one order of magnitude lower than those for the Zr-C ones. Such differences are related to the interfacial bonding mechanism. Our guess is that graphene/borophene layers in the B-C-B structures are coupled by weak physical adsorption, while the Zr-C-Zr ones are connected by strong chemical interaction, similar to that at play in metal/graphene contacts [42]. These hypotheses will be investigated further when discussing the details of the electronic structure in Sec. III E.

In concluding this section we remark our main finding, namely that the interface adhesion energy E_{ad} is strongly affected by the chemical species facing each other across the interface. This, however, also includes the misfit strain energy U_i. When U_i is subtracted from E_{ad} we are left with the interface binding energy E_{b}, which ranks the binding strengths of our interface models as I$_{\text{Zr-C}}$ > II/III$_{\text{Zr-C}}$ > I/II$_{\text{B-C}}$.

C. Interfacial cleavage

The interfacial fracture behavior is investigated by computing the traction-displacement curves, which are obtained from the derivative of the total energy changes upon displacing two materials adjacent to the interface [43]. Calculations are performed for two different displacement modes, namely opening (mode I, the two sides of the interface are displaced along a direction orthogonal to the interface plane) and sliding (mode II, the two sides of the interface are displaced along the interface plane). In this section we will present results for mode I, for which we have adopted the cleavage model from Lazar and Podloucky [44], while the displacement mode II will be discussed in Sec. III D.

In the fracture mode I the trilayer structure is separated by introducing an initial displacement of length z between the top ZrB$_2$ slab and the graphene layer, so that a pre-existing crack is introduced at one side of the interface. Thus, the interlayer distances of the graphene layer with the bottom and top ZrB$_2$ slabs are, respectively, d_0 and $d_0 + z$, where d_0 is the equilibrium interlayer distance calculated previously. The corresponding energy change per unit area defines the cleavage energy E_{c} which writes

$$E_{\text{c}}(z) = \frac{E_{\text{tot}}(d_0 + z) - E_{\text{tot}}(d_0)}{A}.$$
(5)

In Eq. (5) $E_{\text{tot}}(d_0)$ and $E_{\text{tot}}(d_0 + z)$ are the total energies of the equilibrium hybrid structure and of the cleaved one, respectively.

We have then fitted the $E_{\text{c}}(z)$ curves with a Morse function

$$E_{\text{c}}(z) = W_{\text{sep}}[1 - \exp^{-a'z}]^2,$$
(6)

where W_{sep} is the work of separation. Here the parameter a' determines the width of the $E_{\text{c}}(z)$ curve, while $2W_{\text{sep}}(a')^2$ controls its curvature at $z = 0$. The traction curve $\sigma(z)$ is then calculated as the first derivative of $E_{\text{c}}(z)$ with respect to z,

$$\sigma(z) = 20a'W_{\text{sep}}[\exp^{-a'z} - e^{-2a'z}],$$
(7)

where $\sigma(z)$ is in GPa. Then, the interfacial cleavage strength σ_{c} and the critical crack length δ_{c} are defined as the values of σ and z at the maximum of the $\sigma(z)$ curve. The general behaviour of $E_{c}(z)$ is rather simple. As the pre-opening crack grows (z gets larger), E_{c} continuously increases until it reaches its maximum value W_{sep}. Thereafter a crack between free (noninteracting) surfaces is formed. The final separation δ_{f} thus can be written as

$$\delta_{\text{f}} = \frac{2\Delta W_{\text{sep}}}{\sigma_{\text{c}}}.$$
(8)

The typical mode of cleavage used in the calculation is presented in Fig. 4(a) and our calculated cleavage energies are shown in Fig. 4(b) for cleaving across the Zr-C and B-C interfaces. As a comparison, in Fig. 4(c) we show the cleavage energy for cleaving the ZrB$_2$ matrix across the Zr-B and B-B atomic layers, while the traction-separation curves are displayed in Fig. 5. Note that three kinds of structural relaxation strategies are considered when calculating the relevant cleavage quantities, and these are explained in the SI. We start our analysis with the brittle cleavage due to a sharp fracture surface and then we move our attention to the effects of structural relaxation and of the graphene layer corrugation.
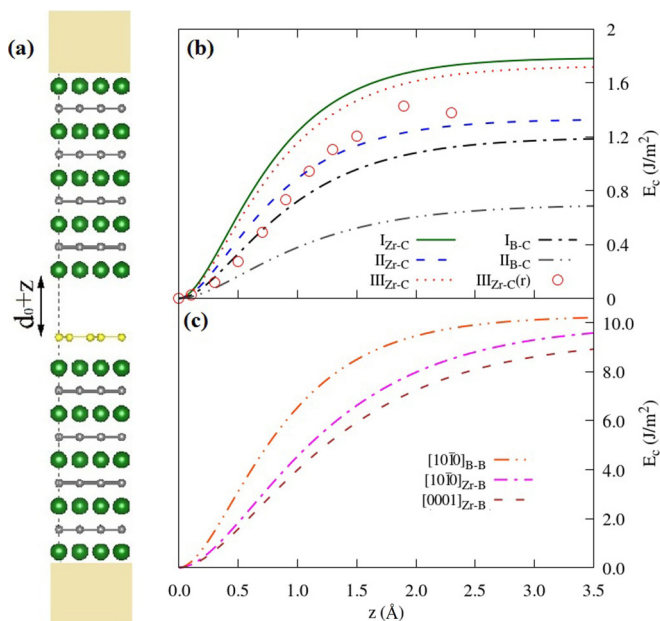
FIG. 4. The cleavage of ZrB_2/graphene composite. (a) A schematic diagram of the cleavage mode applied by adding a pre-opening crack of length z to the equilibrium trilayer structures (color code: green = Zr, gray = B, yellow = C). In (b) we present the energy separation curves $E_c(z)$ for rigid cleaving (no relaxation) of various interface models between Zr and C, and between B and C layers. In (c) the same quantity is plotted for cleaving bulk ZrB_2 between two B planes and between Zr and B planes along $[10\bar{1}0]$ and $[0001]$ directions. In (b) we also report calculations where the atomic positions are relaxed. This is labeled as $III_{Zr-C}(r)$ and the curve must be compared with the one for the same cleavage but obtained without relaxation III_{Zr-C}.
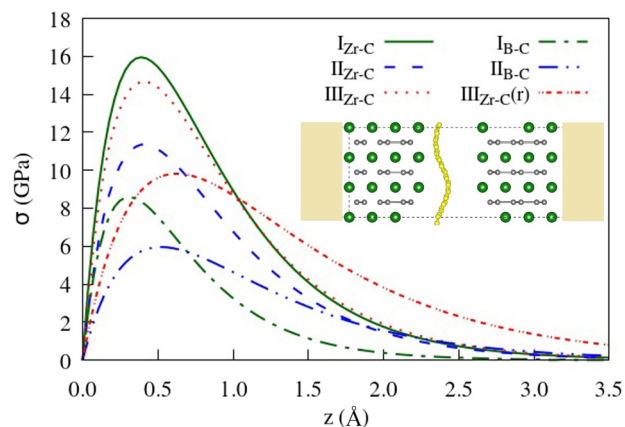

FIG. 5. Traction curves for the cleavage between Zr and C of the interface models I, II, and III, and for the cleavage between B and C of the interfaces I and II. A relaxation case with a rugged fracture graphene surface is labeled as $III_{Zr-C}(r)$, and the atomic structure next to the fracture surface is presented as a ball-and-stick plot in the inset (color code: green = Zr, gray = B, yellow = C).

Among all the cleavage modes, cleaving B-B bonds along $[10\bar{1}0]$ in bulk ZrB_2 has the highest W_{sep} value of 10.29 J/m^2, which is similar to what is found for cleaving between Zr and B both along $[10\bar{1}0]$ and $[0001]$, $W_{sep} \sim 9.50$ J/m^2. In comparison, cleaving across the interfaces with graphene requires W_{sep} values one order of magnitude smaller (in the range 0.70–1.79 J/m^2). This confirms that the ZrB_2/graphene interfaces are the weak part of the structure and can deflect cracks during the fracture of the composites. Such feature allows energy to be released at the ZrB_2/graphene interface, so that the structural integrity of the ZrB_2/graphene composite can be preserved.

In more detail, both W_{sep} and σ_c systematically decrease when going through the interfaces I_{Zr-C}, III_{Zr-C}, II_{Zr-C}, I_{B-C}, and II_{B-C}, namely they follow the ranking obtained for the binding energy curves of Fig. 3. This correspondence has been also observed in the past when studying interfaces in lamellar TiAl alloys [45]. Since the crack is initiated by breaking the interaction at the Zr-C or the B-C contact, the bonding mechanism across the interfaces is responsible for the interface strength. In other words, the values of σ_c, W_{sep}, and E_b all reflect the ease of interfacial debonding. Although in real composites additional features, such as defects and impurities, can modify the strength of the interfacial interaction and then affect the way a crack propagates, the ranking calculated here

already provides a clear map of the strengths of the various components of a graphene/ZrB_2 composite.

Several important parameters, such as the work of separation W_{sep}, the traction strength $\sigma_c = \max[\sigma(z)]$, the critical separation δ_c, and the final separation δ_f, are extracted from these curves and are summarized in Table I. These quantities, together with the shear parameters, also presented in Table I, can then be used as inputs in continuum simulation models of cohesive zone to provide a complete understanding of the interface debonding of GCMC materials. It is worth mentioning that the σ_c values vary from 15.95 to 4.02 GPa when going from I_{Zr-C} to II_{B-C}. This provides the chance of tuning the mechanical behavior of interfaces in GCMCs over one order of magnitude.

We have then investigated the effects of the structural relaxation on the cleavage behavior (a detailed discussion is provided in the SI [35]). The atomic positions within a region 4.5 Å vertical to the cleavage surfaces are relaxed in order to minimize the internal stresses and the total energy. The results are labeled as $III_{Zr-C}(r)$ in Figs. 4(b) and 5, while the final geometry is shown in the inset of Fig. 5, where it is evident that relaxation produces a corrugation of the graphene layer. It is experimentally known that graphene sheets exhibit large corrugations when adsorbed on metal surfaces [41]. This is observed here, since the buckling of graphene can efficiently relieve the misfit strains across the interface and provides an energy reduction channel alternative to misfit dislocations. As illustrated in Fig. 4(b) with the open circles, the corrugation of graphene lowers down W_{sep} by $\sim$0.4 J/m^2. At the same time it makes the critical cleavage stress decreasing from 15 to 10 GPa. This demonstrates that, in general, graphene buckling has the effect of weakening the interface adhesion. The effect originates from the fact that the interface, namely the surface contact between graphene and ZrB_2, is partially detached. Thereby, the contact area is reduced by the corrugation. Note that the calculated rippling period of graphene is constrained by the in-plane dimensions of the supercell, and that the III_{Zr-C}^{AB} supercell (148 atoms) is the largest studied here. One then

TABLE I. Mechanical parameters of ZrB_2 matrix, graphene, and ZrB_2/graphene interface. W_{sep}: work of separation, σ_c: cleavage strength, δ_c: critical separation distance, δ_f: final separation distance, γ_{us}: unstable stacking fault energy, γ_{sf}: stacking fault energy, τ_c: shear strength.

Mode I loading (opening)		W_{sep} (J/m^2)	σ_c (GPa)	δ_c (Å)	δ_f (Å)
ZrB_2	$[10\bar{1}0]_{B\text{-}B}$	10.29	82.16	0.43	2.50
	$[10\bar{1}0]_{Zr\text{-}B}$	9.97	56.06	0.62	3.56
	$[0001]_{Zr\text{-}B}$	9.38	49.54	0.66	3.79
Graphene	$[0001]_{C\text{-}C}$	0.36	2.27	0.55	3.17
Interfaces	$I_{Zr\text{-}C}$	1.79	15.95	0.39	2.24
	$III_{Zr\text{-}C}$	1.73	14.67	0.41	2.35
	$II_{Zr\text{-}C}$	1.33	11.34	0.41	2.35
	$I_{B\text{-}C}$	1.20	8.96	0.46	2.68
	$II_{B\text{-}C}$	0.85	4.02	0.73	4.23
Mode II loading (sliding)		γ_{sf} (J/m^2)	γ_{us} (J/m^2)	τ_c (GPa)	
ZrB_2	$\{0001\}\langle11\bar{2}0\rangle$	–	3.47	49.62	
	$\{0001\}\langle10\bar{1}0\rangle$	3.03	3.47	24.45	
Graphene	armchair	–	0.09	1.00	
	zigzag	–	0.04	0.48	
Interfaces	$I_{Zr\text{-}C}$ $\{0001\}\langle11\bar{2}0\rangle$	–	0.57	4.55	
	$I_{Zr\text{-}C}$ $\{0001\}\langle10\bar{1}0\rangle$	0.05	0.57	8.37	
	$I_{B\text{-}C}$ $\{0001\}\langle11\bar{2}0\rangle$	0.04	0.10	1.87	
	$I_{B\text{-}C}$ $\{0001\}\langle10\bar{1}0\rangle$	0.04	0.15	3.35	

has to expect that for planar structures with an even larger in-plane cell and consequently smaller lattice misfit and internal stress, the effect of graphene buckling will be in general less pronounced.

D. Interface sliding

In order to extract the traction-separation curves under the loading mode II [43] we now study the associated interfacial sliding process. This is modeled by displacing the top ZrB_2 slab along certain directions parallel to the interface plane, while monitoring the change in the total energy as a function of the sliding vectors. The sliding energy profile γ can be plotted as the change in total energy (per unit area) with respect to the energy of the undistorted structure as a function of the sliding vector, namely

$$\gamma = \left(E_{tot}^{sh} - E_{tot}^0\right)/A, \qquad (9)$$

where E_{tot}^0 and E_{tot}^{sh} are the total energies of the equilibrium and of the distorted structure, respectively.

The *rigid* energy landscape is derived by monitoring the energy of the distorted structure without performing any structural relaxation. In addition, we have also calculated the effects of full structural relaxation by using the nudged elastic band (NEB) method [46,47]. In practice we allow atomic relaxation both perpendicular to the gliding plane and in-plane. At the same time the minimum energy path (MEP) is tracked down, while keeping the Burgers vectors fixed. This fully relaxed calculations have been performed only for the interface models $I_{Zr\text{-}C}$ (86 atoms in the supercell) and $I_{B\text{-}C}$ (89 atoms). As for the interface types II and III (118 and 148 atoms, respectively), only the rigid sliding profiles have been studied because of the heavy computational costs associated to the DFT-based NEB method. The shear stress along a given

direction x is then calculated as the slope of the energy profile along that direction, namely

$$\tau_x = \frac{d\gamma}{dx}, \qquad (10)$$

where the maximum τ is defined as the interfacial shear strength $\tau_c^x = \max\{\tau_x\}$.

Five slip systems are studied, namely basal $\langle a \rangle$: (0001) $\langle\bar{1}2\bar{1}0\rangle$, basal $\langle b \rangle$: (0001)$\langle10\bar{1}0\rangle$, prismatic $\langle a \rangle$: $(10\bar{1}0)\langle\bar{1}2\bar{1}0\rangle$, prismatic $\langle c \rangle$: $(10\bar{1}0)\langle0001\rangle$, and prismatic $\langle a + c \rangle$: $(10\bar{1}0)$ $\langle11\bar{2}3\rangle$. They are associated with the interfaces of type I and III with $[0001]_{ZrB_2}$ and $[10\bar{1}0]_{ZrB_2}$ orientation, respectively. The equilibrium geometry of the Zr-C-Zr structures has an AB stacking sequence, while that of the B-C-B structure is AA type.

The top panels of Fig. 6 display the energy profiles for rigid sliding along the Zr-C-Zr interfaces. In general, the energy barriers are observed to be relatively small in magnitude (< 0.15 J/m^2). In addition, we find that the sliding curves present a number of maxima and minima, marked in the figures by arrows. These correspond to different stacking configurations of the supercell (also indicated in the figure), which are encountered during the sliding process. As the different stacking orders have a rather similar binding energy (see Sec. III B 2), we expect the sliding energy profile to be relatively shallow, as confirmed by the results shown here.

Then, the traction curves for mode II are derived as numerical derivative of the corresponding sliding energy profiles and they are presented in the bottom panels of Fig. 6. For basal sliding, namely the slips along $\langle\bar{1}2\bar{1}0\rangle_{ZrB_2}$ and $\langle10\bar{1}0\rangle_{ZrB_2}$ of the $I_{Zr\text{-}C}$ interface, the shear strengths are calculated as 1.47 and 0.74 GPa, respectively. In contrast, those along $\langle\bar{1}2\bar{1}0\rangle_{ZrB_2}$, $\langle0001\rangle_{ZrB_2}$, and $\langle11\bar{2}3\rangle_{ZrB_2}$ for interface $III_{Zr\text{-}C}$ are, respectively, 1.15, 1.13, and 0.66 GPa. Therefore, the slip
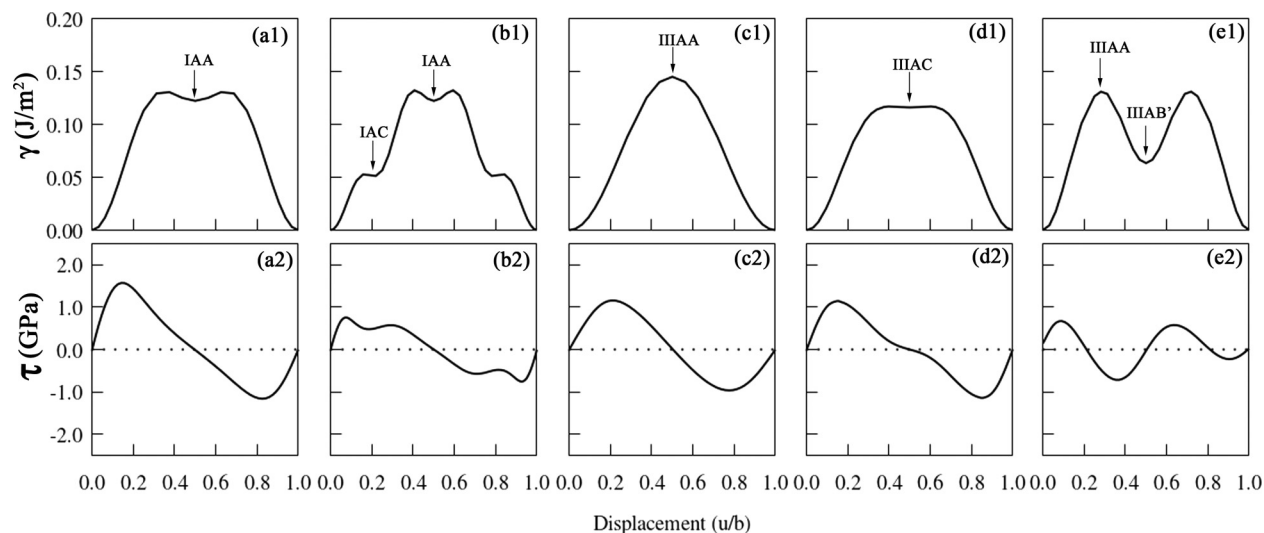
FIG. 6. Rigid energy landscapes (upper panels) γ and corresponding shear stress (lower panels) τ as a function of the displacement. A displacement vector $\vec{u}$ is measured with respect to the relevant Burgers vector $|\vec{b}|$. The Burgers vectors in (a) through (e) are, respectively, $\vec{b}_1 = \frac{1}{3}\langle \bar{1}2\bar{1}0 \rangle_{ZrB_2}$, $\vec{b}_2 = \langle 10\bar{1}0 \rangle_{ZrB_2}$, $\vec{b}_3 = \frac{1}{3}\langle \bar{1}2\bar{1}0 \rangle_{ZrB_2}$, $\vec{b}_4 = \langle 0001 \rangle_{ZrB_2}$, and $\vec{b}_5 = \frac{1}{3}\langle 11\bar{2}3 \rangle_{ZrB_2}$.

system $\{10\bar{1}0\}\langle 11\bar{2}3 \rangle_{ZrB_2}$ is prone to be activated first. The easy activation of the $\{10\bar{1}0\}\langle 11\bar{2}3 \rangle_{ZrB_2}$ slip system was previously reported [48] for bulk ZrB_2 at temperatures over $700\,^\circ$C. The interfacial sliding along $\langle \bar{1}2\bar{1}0 \rangle_{ZrB_2}$ of I_{Zr-C} shows comparable shear strengths to those of $\langle 0001 \rangle_{ZrB_2}$ and $\langle 11\bar{2}0 \rangle_{ZrB_2}$ of III_{Zr-C}, although the latter two exhibit slightly lower values.

In order to trace the the sliding energy profile along the minimum energy path, we perform full relaxation calculations using the NEB method. This also allows us to extract some key shear parameters. The energy maximum, namely the unstable stacking fault energy γ_{us}, governs the dislocation nucleation at sites of stress concentration such as at the crack tips. The metastable points (local energy minima) correspond to stable stacking faults with their energies γ_{sf} determining the dislocation core dissociation, the Peierls stress, the dislocation energy, and the primary slip planes. These shear parameters γ_{us} and γ_{sf} are summarized in Table I.

The relaxed sliding energy profiles are then shown in Figs. 7(a) and 7(b) for the interfaces I_{Zr-C} and I_{B-C}, respectively. Let us look at the I_{Zr-C} case [Fig. 7(a)] first. We find that γ_{us} for both the basal $\langle \bar{1}2\bar{1}0 \rangle_{ZrB_2}$ and $\langle 10\bar{1}0 \rangle_{ZrB_2}$ shear is 0.57 J/m^2, a value that is almost four times larger than those
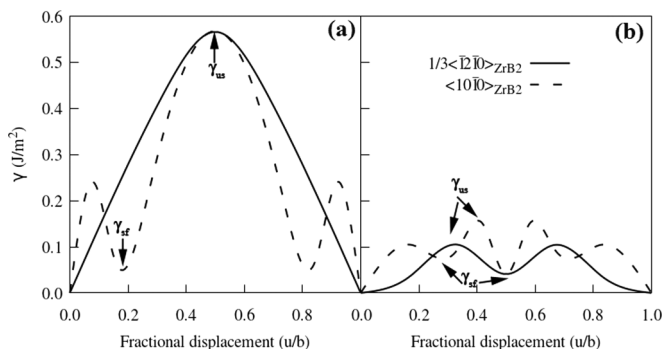

FIG. 7. Energy profiles of the interfacial sliding obtained by allowing full atomic relaxation (NEB method): (a) I_{Zr-C} and (b) I_{B-C}. The Burgers vectors are $\vec{b}_1 = \frac{1}{3}\langle \bar{1}2\bar{1}0 \rangle_{ZrB_2}$ and $\vec{b}_2 = \langle 10\bar{1}0 \rangle_{ZrB_2}$.

obtained for rigid shearing. This increase is due to the atomic rearrangement, especially the out-of-plane corrugation of the graphene layer, which effectively obstructs the interfacial sliding. In order to understand such dramatic increase we note that the total energy reduction due to atomic relaxation differs depending on the precise stacking order. In the case of Zr-C interface, the AB stacking corresponds to the initial position of its sliding energy landscape (see Fig. 6), which shows a deeper energy well after atomic relaxation since some of the stress is released. In contrast, the AA configuration is at a peak of the γ curve and it is relatively stress-free because of the symmetric configuration. As a consequence atomic relaxation has little effect on its energetics. Thus, the final result of the relaxation is that of increasing the energy barrier ($\gamma_{us} = E_{AA} - E_{AB}$). This suggests that the role of graphene corrugation is twofold. On the one hand, it reduces the interface adhesion strength during the interface debonding. On the other hand, before detaching, it increases the interfacial friction during the sliding process.

Moving to the I_{B-C} interface, we note that the γ_{us} values (0.10–0.15 J/m^2) are similar to those calculated without performing atomic relaxation. Now γ_{us} is four times smaller than that of I_{Zr-C}. This is the result of the shallow behavior of γ for the I_{B-C} interface, consistent with the ranking given before for the adhesive and binding energies. Since the B-C-B structures are bonded by weak interaction (see later discussion), also their low energy states have the symmetric AA stacking, rather than the nonsymmetric AB or AC ones. Graphene corrugation has little effect on the interfacial sliding of B-C interfaces, when compared to the case of the Zr-C ones. We then conclude that the B-C-B structures are much more favorable to sliding that the more adhesive Zr-C-Zr ones.

Finally, we compare the ideal shear strength of the Zr-C-Zr and B-C-B structures with that of the bulk ZrB_2 matrix. The calculated τ_c for I_{Zr-C} are 4.55 and 8.37 GPa, when sliding respectively along $\vec{b}_1 = \frac{1}{3}\langle \bar{1}2\bar{1}0 \rangle_{ZrB_2}$ and $\vec{b}_2 = \langle 10\bar{1}0 \rangle_{ZrB_2}$. The same quantities are reduced to 1.87 and 3.35 GPa for the corresponding I_{B-C} interface and they
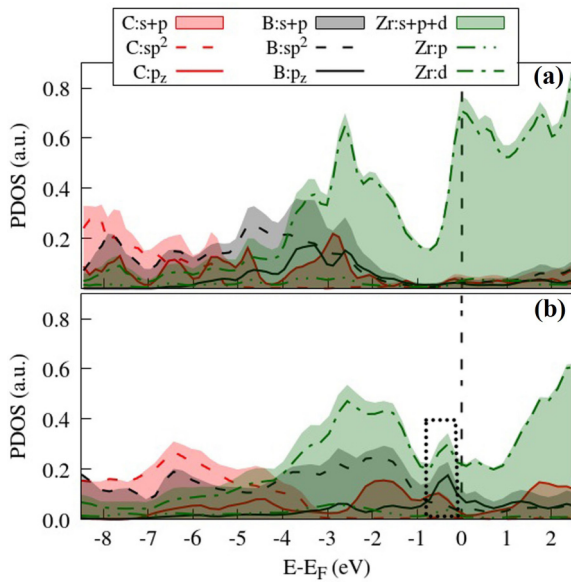
FIG. 8. Projected density of states (PDOS) over the C atoms in graphene, and the Zr and B ions in the ZrB_2 plane next to the graphene sheet for the interface models (a) I_{Zr-C} and (b) I_{B-C}.

FIG. 9. 3D isosurface plots of the charge density difference between that of the ZrB_2/graphene structure and those of the constituent parts (the ZrB_2 slabs and the graphene layer). The isosurfaces are taken at a density value of ± 0.003 e/bohr^3 (electron accumulation in cyan and electron depletion in yellow). We consider the trilayered models: (a) I_{Zr-C} and (b) I_{B-C}. (c) The partial charge density of the I_{B-C} junction originating from the states corresponding to the π orbitals near E_F in the PDOS (the black box in Fig. 8). Color code: green = Zr, gray = B, red = C.

are increased to 49.62 and 24.45 GPa for bulk ZrB_2. Thus the interfacial shear strength of ZrB_2/graphene interfaces is at least one order of magnitude lower than those of the ZrB_2 matrix. The same observation is valid for the cleavage strength. This suggests that the γ surfaces are much less corrugated at a heterophase interface, which indicates relatively ease of interfacial sliding. When examining specific interfaces, it is clear that I_{B-C} is more prone to host deformation pathways than I_{Zr-C}.

E. Interfacial bonding mechanism

One of the main results from the previous sections is that the Zr-C-Zr and B-C-B structures present very different strengths of adhesion and binding, as well as traction strengths under the two loading modes investigated. This suggests that different bonding mechanisms are at play in Zr-C and B-C interfaces. Here we analyze the interfacial interaction by looking at the projected density of states (PDOSs), the charge density, the projected charge density, the band structures, and the local electrostatic potential.

Let us begin by looking at the PDOS over the carbon atoms of the I_{Zr-C} structure, presented in Fig. 8(a), which suggests a covalent bonding character for the Zr-C interface. As expected, the partially filled Zr d bands dominate the PDOS for energies starting at 4 eV below the Fermi level E_F. They represent the main contribution to the Fermi surface for Zr-C-Zr structures. In this case a distinctive feature is the appearance of a PDOS reduction at about 1 eV below E_F, which separates a region ($E > E_F - 1$ eV) with little contribution from either B or C, from another region ($E < E_F - 1$ eV), where the PDOS from the C $2p_z$ orbital is significant. This is a clear signature of the strong hybridization between the C $2p_z$ and the Zr $4d$ orbitals, and the consequent formation of Zr-C covalent bonds. Such attribution is consistent with the
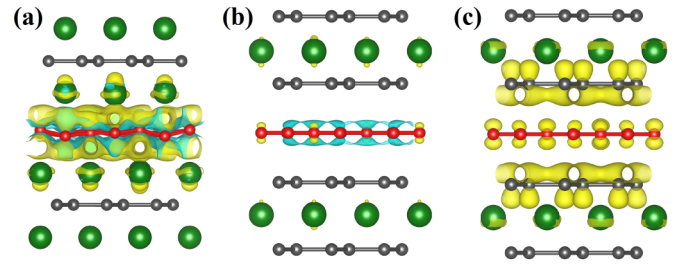
strong affinity between Zr and C and the existence of covalent ZrC_{1-x} compounds. Covalent bonding across interfaces has also been suggested for the interfaces of Ti_2C/graphene [40], ZrC/SiC [49], and metal graphene contacts [42].

Such picture of a strong covalent bond is confirmed by looking at the difference in charge density between that of the Zr-C-Zr junction and those of the individual components (the ZrB_2 slabs and the graphene monolayer), presented in Fig. 9(a). We observe electron accumulation (cyan surface) in the graphene plane and also in the interstitial regions between the Zr and C atoms. At the same time there is electron depletion (yellow surface) over the Zr planes. This points to a significant charge transfer from the Zr surfaces of ZrB_2 to graphene, which contributes to the ionic component of the bonding at the interface. The net atomic charges (NACs), as calculated from Bader analysis, further confirm such observation. In bulk ZrB_2, the NACs of Zr and B are $+1.54$ e and -0.77 e, respectively [50] (e is the electron charge). These become $+1.23$ e (Zr) and -0.35 e (C) at the Zr-C interface. Similar results are obtained by using atomic charges computed with the DDEC6 approach [51–53] (see results in Fig. S2 of the SI), although the precise absolute values between the two methods are, as expected, slightly different. We then conclude that the interfacial Zr-C bonding has a mixed ionic/covalent nature.

The situation for the B-C-B structures is rather different, as one can easily conclude by looking at Fig. 8(b). In this case the most prominent feature of the PDOS is a peak just below the Fermi level, with significant projections originating from the B and C $2p_z$ orbitals. This suggests that the bonding might have a π-π stacking nature, as commonly present in aromatic compounds [54]. Again the charge density distribution confirms our hypothesis. Figure 9(b) shows the charge density difference between the B-C-B structure and its constituent components and demonstrates that there is some minor charge accumulation on the π orbitals of graphene. However, we do not find a distinct region of charge depletion (it is not evident for the isosurface value of 0.003 e/bohr^3 used in the plot), which instead takes place uniformly across the ZrB_2 slab.
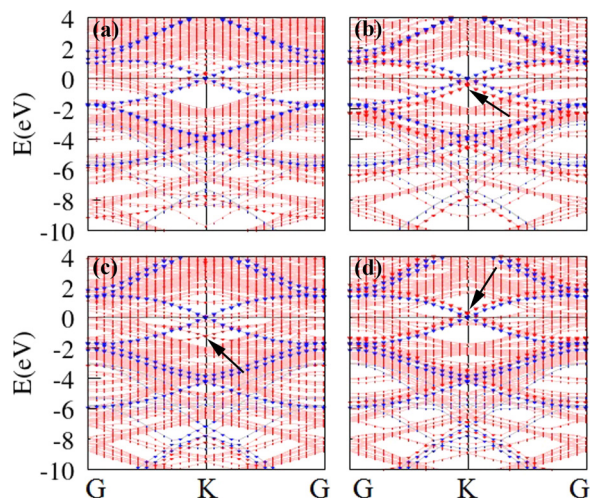
FIG. 10. Electronic band structure of graphene in the (a) I_{Zr-C} and (c) I_{B-C} interface models. The red dots represent the intensity of π-orbital components of the bands. The blue bands correspond to an isolated graphene layer with the size of the dots having the same meaning. The arrows indicate the position of the Dirac point. In (b) and (d) we show the bands of (b) I_{Zr-C} and (d) I_{B-C} heterostructures, where now the distance between graphene and the ZrB_2 slabs is kept artificially at 5 Å.

The NAC analysis performed with either the Bader and the DDEC6 approach returns a similar picture.

Additional information on the electronic structure of the various interfaces can be obtained by looking at the electronic band structure of the supercells and the planar average of their electrostatic potentials. Let us discuss the band structure first. Figure 10 shows the band structure of the Zr-C-Zr and B-C-B trilayers, calculated both at the equilibrium distance [Figs. 10(a) and 10(c), respectively] and at the artificial distance of 5 Å [Figs. 10(b) and 10(d), respectively]. This allows us to track the position of the various bands as the two interfaces form. The bands corresponding to the heterostructures are in red and the size of the symbols is proportional to the C-π character of the band. In every panel we also report the band structure of isolated graphene (blue bands and same convention about the size of the symbols). At large separation it is always easy to identify the graphene Dirac point, which is positioned at around E_F for both the Zr-C-Zr

[Fig. 10(b)] and the B-C-B [Fig. 10(d)] structure. However, as the distance between graphene and the ZrB_2 slabs gets smaller the two junctions behave differently. On the one hand, for the B-C-B configuration the Dirac point remains clearly visible below the Fermi level [see arrow in Fig. 10(b)], indicating that the bonding is not strong enough to perturb significantly the graphene π band and that graphene is actually slightly n doped in the junction. On the other hand, for the Zr-C-Zr stack the energy downshift of the graphene π bands is much more significant and there is no longer a clear evidence of the new position of the Dirac point [Fig. 10(a)]. This means that the graphene π band is now strongly hybridized with the ZrB_2 band structure.

The planar averages of the electrostatic potential along the junction stack, Fig. 11, confirm the picture offered by the band structures. In fact, for both structures we find that the electrostatic potential at the graphene layer is lower than that of isolated graphene, once the vacuum levels of the two systems are lined up. This means that the graphene layer is n doped in both heterostructures. Such effect is significantly more pronounced for the Zr-C termination than for the B-C one, confirming the conclusions made before when discussing the PDOS and the charge density distributions.

IV. DISCUSSION

The results presented in the previous sections convincingly demonstrate that the Zr-C interfaces display adhesion, cleavage, and shear strength superior to those of the B-C ones. This can be well rationalized by noting that the interfacial bonding mechanism is different for the two interface types, covalent for Zr-C and π-π stacking for B-C. The stronger Zr-C interfaces thus present a higher resistance to both crack propagation and interfacial sliding, while the weaker B-C ones allow easy interfacial debonding and shear deformation.

It is important to note that the toughening of a ceramic matrix via graphene nanofillers is correlated to the interface debonding mechanics. In composites interfacial debonding favors energy dissipation via crack bridging, crack deflection, and fillers pulling-out. Thus the distribution of filler/matrix interfaces will uniquely determine the mechanical properties of the final composite. Here we have demonstrated that the two most chemically different ZrB_2 surfaces, namely the Zr- and B-terminated (0001), have a bonding energetics
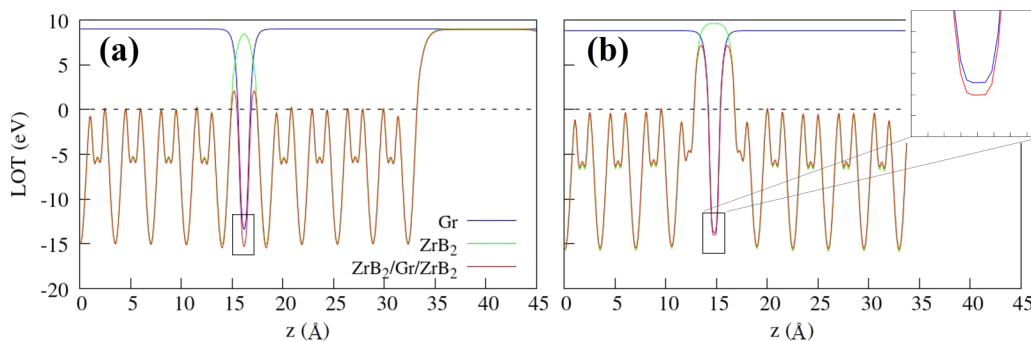

FIG. 11. Planar average of the electrostatic potential (LOT, eV) for the (a) I_{Zr-C} and (b) I_{B-C} interface models. These are compared with those of an isolated graphene layer (in blue) and of a ZrB_2 slab (in green) once the vacuum levels have been aligned. The inset in (b) shows a magnification of the interface B-C-B region.

varying over approximately an order of magnitude. This means that changing the relative distribution of such surfaces in a composite can alter significantly the mechanical response, an evidence that correlates well with the observed wide variation of the K_{IC} values of graphene-reinforced composites [55]. It is also important to know that chemically and structurally different interfaces can be stabilized in ZrB_2 by appropriately tuning the chemical environment during growth [35]. This suggests that the growth parameters of the ZrB_2 matrix can be used as a tool for designing the mechanical properties of the final graphene-reinforced composite.

Finally, we note that, monolithic ZrB_2 and graphene nanoplatelets are usually employed as starting materials during the spark plasma sintering [7] of ZrB_2/graphene composites. The nanoplatelets are made of short stacks of ribbon-shaped graphene sheets. These are functionalized with groups like ethers, carboxyls, or hydroxyls, which can further modify the interfacial bonding details [56]. Therefore, a scrupulously designed surface treatment of graphene can be an additional tool for controlling the interfacial interaction, and hence the interface mechanics and the failure modes of GCMC materials.

In closing this section we wish to take a further look at the B-C interfaces and compare their mechanical properties to those of graphite. In particular, it appears that the B-C π-π interaction is stronger than the van der Waals coupling between graphene layers and, in general, among monolayers of van der Waals layered compounds. This is demonstrated in Fig. 12(a), where we compare the binding energy curves $E_b(d_i)$ of the B-C-B structures with that of graphene. The binding energies are calculated to be 0.488 and 0.663 J/m^2 for I_{B-C} and II_{B-C}, respectively. In contrast we compute $E_b(d_0) = 0.374$ J/m^2 for a six-layer graphene nanosheet. In addition, the equilibrium interlayer distance at the B-C interfaces is between 2.5 and 3.0 Å, while that in graphite is 3.23 Å. This all points to say that the π-π stacking interaction here is stronger than that between graphene layers. There are two reasons behind this difference: (1) there is some electrostatic interaction between graphene and the boraphene layers; and (2) there is an offset stacking between boraphene and graphene contributing to reduce the repulsive interaction. The difference between the layers interaction in graphene/boraphene and graphene/graphene manifests itself in the sliding energy profiles illustrated in Fig. 12(b). We find that the γ_{us} values for graphene are 0.04 and 0.09 J/m^2, respectively, for shearing along the zigzag and armchair edges. The slipping along the basal $\langle\bar{1}2\bar{1}0\rangle_{ZrB_2}$ and $\langle10\bar{1}0\rangle_{ZrB_2}$ directions returns the γ_{us} values of 0.10 and 0.15 J/m^2, respectively. In summary it appears that the B-C bonding strength and its mechanical response to shearing are stronger than those found between graphene sheets in graphene.

V. CONCLUSION

In this work we have studied the heterophase interfaces of graphene-reinforced ZrB_2 composites based on DFT calculations. A number of atomistic models for the various possible interfaces has been constructed by using the thermodynamically most stable surfaces of the ZrB_2 matrix. Then, we have systematically investigated their interface adhesion, mechani-
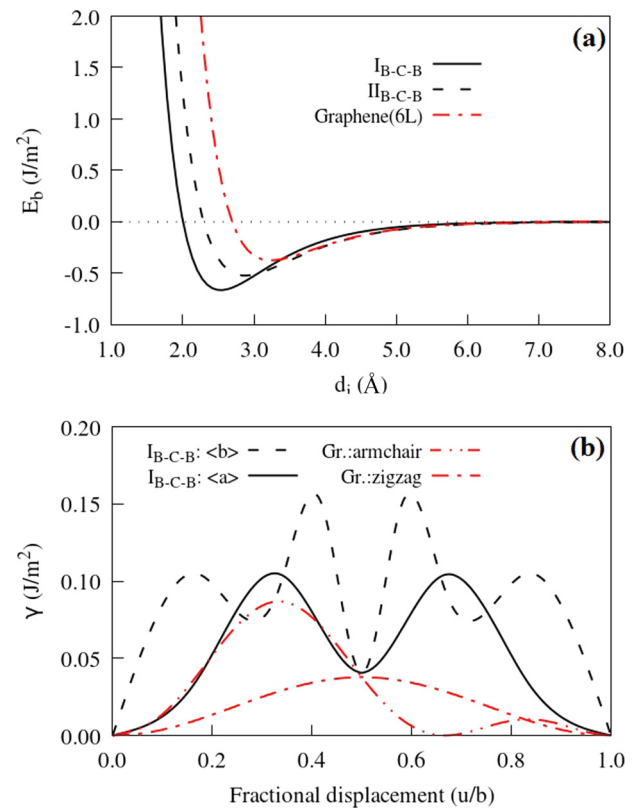

FIG. 12. Comparison of the mechanical properties of the B-C-B structure with that of graphene. (a) Binding energy E_b (in J/m^2) and (b) sliding energy corrugation γ (in J/m^2). In the case of graphene the sliding modes are along the armchair and zigzag directions, while for ZrB_2/graphene we consider displacements along the basal $\langle\bar{1}2\bar{1}0\rangle_{ZrB_2}$ ($\langle a\rangle$) and $\langle10\bar{1}0\rangle_{ZrB_2}$ ($\langle b\rangle$) directions.

cal behavior, and bonding mechanism. We have demonstrated that two kinds of interfaces, namely Zr-C and B-C, offer a wide spectrum of mechanical properties due to their dissimilar interaction between the constituent materials. In particular Zr-terminated surfaces bind to graphene in a covalent way, while the interaction with the borophene planes in ZrB_2 has a π-π-stacking nature. By tuning the surface chemistry of the ZrB_2 matrix one can prepare composites that expose graphene predominantly to a specific ZrB_2 surface (either Zr or B or mixed termination), so it is possible to go from a regime of weak graphene/matrix interaction to one where the interaction is relatively strong. This provides an important design scheme in the synthesis of ceramic composites. Finally, we have analyzed the role of graphene rippling over the mechanical properties of the interfaces. Interestingly we have found that rippling drastically increases the friction for sliding graphene over ZrB_2 in the case of Zr-C-Zr contacts, while it has no significant effect for that with B-C-B ones.

TABLE II. Structural parameters of the various $ZrB_2/Gr/ZrB_2$ (Gr = graphene) interface structures investigated.

Heterostructures			Interlayer	In-plane	Lateral strain (%)	
Interface	Composition	ZrB_2 slab	d_i	a_i/b_i (A)	Δa_{Gr} (Δb_{Gr})	Δa_{ZrB_2} (Δb_{ZrB_2})
I_{Zr-C}^{AA}	$(Zr_3B_6)_8C_8Zr_6$	$\sqrt{3} \times \sqrt{3}(0001)$	2.30	5.422	10.2	-1.0
I_{Zr-C}^{AB}	$(Zr_3B_6)_8C_8Zr_6$	$\sqrt{3} \times \sqrt{3}(0001)$	2.27	5.422	10.2	-1.0
II_{Zr-C}^{AA}	$(Zr_4B_8)_8C_{14}Zr_8$	$2 \times 2(0001)$	2.35	6.355	-1.7	0.5
II_{Zr-C}^{AB}	$(Zr_4B_8)_8C_{14}Zr_8$	$2 \times 2(0001)$	2.35	6.355	-1.7	0.5
II_{Zr-C}^{AC}	$(Zr_4B_8)_8C_{14}Zr_8$	$2 \times 2(0001)$	2.30	6.355	-1.7	0.5
III_{Zr-C}^{AA}	$(Zr_6B_{12})_6C_{28}Zr_{12}$	$2 \times 3(10\bar{1}0)$	2.38	6.419/10.637	-2.5 (-5.2)	1.5 (1.5)
$III_{Zr-C}^{AB'}$	$(Zr_6B_{12})_6C_{28}Zr_{12}$	$2 \times 3(10\bar{1}0)$	2.35	6.419/10.637	-2.5 (-5.2)	1.5 (1.5)
III_{Zr-C}^{AB}	$(Zr_6B_{12})_6C_{28}Zr_{12}$	$2 \times 3(10\bar{1}0)$	2.35	6.419/10.637	-2.5 (-5.2)	1.5 (1.5)
I_{B-C}^{AA}	$(Zr_3B_6)_8C_8$	$\sqrt{3} \times \sqrt{3}(0001)$	2.50	5.422	10.2	-1.0
I_{B-C}^{AB}	$(Zr_3B_6)_8C_8$	$\sqrt{3} \times \sqrt{3}(0001)$	2.32	5.422	10.2	-1.0
II_{B-C}^{AA}	$(Zr_4B_8)_8C_{14}$	$2 \times 2(0001)$	2.90	6.355	-1.7	0.5
II_{B-C}^{AB}	$(Zr_4B_8)_8C_{14}$	$2 \times 2(0001)$	3.00	6.355	-1.7	0.5

Rui Dong for the CLATTICE code to implement the coincidence lattice method.

APPENDIX

We have summarized the structural parameters of all the interfaces examined in this work in Table II. These include the composition, the in-plane size of the ZrB_2 slabs, the in-plane lattice parameters (a_i, b_i), the interlayer distances (d_i), and the in-plane misfit strains (Δ_{ZrB_2} or Δ_G) for both the ZrB_2 matrix and the graphene (Gr) layer. Since ZrB_2 and graphene are constrained to have common lateral lattice parameters (a_i and b_i), the misfit strains in ZrB_2 and graphene are respectively defined as

$$\Delta_{ZrB_2} = \left(\frac{a_i}{a_{ZrB_2}} - 1 \right) \times 100\%,$$

$$\Delta_{Gr} = \left(\frac{a_i}{a_{Gr}} - 1 \right) \times 100\%. \qquad (A1)$$

where a_{ZrB_2} and a_{Gr} correspond to the lattice parameters of bulk ZrB_2 and graphene, respectively.

More specifically, the atomic structures of each interface models have the following characteristics:

(1) I_{Zr-C}^{AA} and I_{Zr-C}^{AB} [86 atoms with chemical composition $(Zr_3B_6)_8C_8Zr_6$] have Zr-C-Zr bonding across both

interfaces. They have the same in-plane arrangement as the Ni(111)/graphene interface shown in Fig. 1(b) of Ref. [42]. The supercells are made of two fragments of the $\sqrt{3} \times \sqrt{3}$ (0001) ZrB_2 slab, sandwiching a graphene monolayer rotated by $30°$ with respect to the ZrB_2 borophene plane [see Figs. 1(b) and 1(e)].

(2) I_{B-C}^{AA} and I_{B-C}^{AB} [89 atoms with composition $(Zr_3B_6)_9C_8$], displayed in Figs. 1(h) and 1(k), are similar to I_{Zr-C}^{AA} and I_{Zr-C}^{AB}, except that the interfaces are B-C-B type.

(3) II_{Zr-C}^{AA}, II_{Zr-C}^{AB}, and II_{Zr-C}^{AC} [118 atoms with composition $(Zr_4B_8)_8C_{14}Zr_8$], shown in Figs. 1(c), 1(f), and 1(i), are built from two blocks of the $2 \times 2(0001)$ ZrB_2 slab and one graphene monolayer. Here the graphene is rotated by $19.1°$ with respect to the ZrB_2 boraphene plane. They have the Zr-C-Zr $[0001]_{ZrB_2}$ stack similarly to I_{Zr-C}^{AA} and I_{Zr-C}^{AB}. However, the Zr atoms are misaligned with the C atoms in graphene, resulting in a smaller lattice mismatch (2% against 10%).

(4) II_{B-C}^{AA} and II_{B-C}^{AB} [110 atoms with composition $(Zr_4B_8)_8C_{14}$] are similar to II_{Zr-C}^{AA} and II_{Zr-C}^{AB}, except that the interface structure is B-C-B type [see Figs. 1(l) and 1(m)].

(5) III_{Zr-C}^{AA}, III_{Zr-C}^{AB}, and $III_{Zr-C}^{AB'}$ [148 atoms with composition $(Zr_6B_{12})_6C_{28}Zr_{12}$], shown in Figs. 1(d), 1(g), and 1(j), are constructed from the 2×3 $(10\bar{1}0)$ surface slab and one graphene monolayer. They have the Zr-C-Zr $[10\bar{1}0]_{ZrB_2}$ termination, and the Zr atoms are misaligned with respect to the C atoms in graphene.

[1] I. A. Kinloch, J. Suhr, J. Lou, R. J. Young, and P. M. Ajayan, Composites with carbon nanotubes and graphene: An outlook, Science **553**, 547 (2018).

[2] H. Porwal, S. Grasso, and M. J. Reece, Review of graphene-ceramic matrix composites, Adv. Appl. Ceram. **112**, 443 (2013).

[3] V. Singh, D. Joung, L. Zhai, S. Das, S. I. Khondaker, and S. Seal, Graphene based materials: Past, present and future, Prog. Mater. Sci. **56**, 1178 (2011).

[4] L. S. Walker, V. R. Marotto, M. A. Rafiee, N. Koratkar, and E. L. Corral, Toughening in graphene ceramic composites, ACS Nano **5**, 3182 (2011).

[5] L. Tao, S. Theruvakkattil Sreenivasan, and R. Shahsavari, Interlaced, nanostructured interface with graphene buffer layer reduces thermal boundary resistance in nano/microelectronic systems, ACS Appl. Mater. Interfaces **9**, 989 (2017).

[6] C. Gao, P. Feng, S. Peng, and C. Shuai, Carbon nanotube, graphene and boron nitride nanotube reinforced bioactive ceramics for bone repair, Acta Biomater. **61**, 1 (2017).

[7] G. B. Yadhukulakrishnan, S. Karumuri, A. Rahman, R. P. Singh, A. Kaan Kalkan, and S. P. Harimkar, Spark plasma sintering of graphene reinforced zirconium diboride ultra-high temperature ceramic composites, Ceram. Int. **39**, 6637 (2013).

[8] Y. An, J. Han, X. Zhang, W. Han, Y. Cheng, P. Hu, and G. Zhao, Bioinspired high toughness graphene/ZrB_2 hybrid composites with hierarchical architectures spanning several length scales, Carbon N.Y. **107**, 209 (2016).

[9] Y. An, X. Xu, and K. Gui, Effect of SiC whiskers and graphene nanosheets on the mechanical properties of ZrB_2-SiC_w-Graphene ceramic composites, Ceram. Int. **42**, 14066 (2016).

[10] P. Miranzo, C. Ramírez, B. Román-Manso, L. Garzón, H. R. Gutiérrez, M. Terrones, C. Ocal, M. I. Osendi, and M. Belmonte, In situ processing of electrically conducting graphene/SiC nanocomposites, J. Eur. Ceram. Soc. **33**, 1665 (2013).

[11] A. Nieto, D. Lahiri, and A. Agarwal, Graphene NanoPlatelets reinforced tantalum carbide consolidated by spark plasma sintering, Mater. Sci. Eng. A **582**, 338 (2013).

[12] J. Liu, Y. Yang, H. Hassanin, N. Jumbu, S. Deng, Q. Zuo, and K. Jiang, Graphene-alumina nanocomposites with improved mechanical properties for biomedical applications, ACS Appl. Mater. Interfaces **8**, 2607 (2016).

[13] B. Liu, J. Wang, F. Li, L. Sun, J. Wang, and Y. Zhou, Investigation of native point defects and nonstoichiometry mechanisms of two yttrium silicates by first-principles calculations, J. Am. Ceram. Soc. **96**, 3304 (2013).

[14] O. T. Picot, V. G. Rocha, C. Ferraro, N. Ni, E. D'Elia, S. Meille, J. Chevalier, T. Saunders, T. Peijs, M. J. Reece, and E. Saiz, Using graphene networks to build bioinspired self-monitoring ceramics, Nat. Commun. **8**, 14425 (2017).

[15] J. Ru, Y. Fan, W. Zhou, Z. Zhou, T. Wang, R. Liu, J. Yang, X. Lu, J. Wang, C. Ji, L. Wang, and W. Jiang, Electrically conductive and mechanically strong graphene/mullite ceramic composites for high-performance electromagnetic interference shielding, ACS Appl. Mater. Interfaces **10**, 39245 (2018).

[16] D. Sciti, L. Silvestroni, F. Monteverde, A. Vinci, and L. Zoli, Introduction to H2020 project C3HARME - next generation ceramic composites for combustion harsh environment and space, Adv. Appl. Ceram. **117**, s70 (2018).

[17] N. P. Padture, Advanced structural ceramics in aerospace propulsion, Nat. Mater. **15**, 804 (2016).

[18] F.-Z. Dai and Y. Zhou, Reducing the ideal shear strengths of ZrB_2 by high efficient alloying elements (Ag, Au, Pd and Pt), Sci. Rep. **7**, 43416 (2017).

[19] L. Zoli, A. Vinci, P. Galizia, C. Melandri, and D. Sciti, On the thermal shock resistance and mechanical properties of novel unidirectional UHTCMCs for extreme environments, Sci. Rep. **8**, 9148 (2018).

[20] P. Hu, W. Guolin, and Z. Wang, Oxidation mechanism and resistance of ZrB_2-SiC composites, Corros. Sci. **51**, 2724 (2009).

[21] H. Hatta, K. Goto, and T. Aoki, Strengths of C/C composites under tensile, shear, and compressive loading: Role of interfacial shear strength, Compos. Sci. Technol. **65**, 2550 (2005).

[22] B. W. Sheldon and W. A. Curtin, Nanoceramic composites: Tough to test, Nat. Mater. **3**, 505 (2004).

[23] J. Kabel, P. Hosemann, Y. Zayachuk, D. E. J. Armstrong, T. Koyanagi, Y. Katoh, and C. Deck, Ceramic composites: A review of toughening mechanisms and demonstration of micropillar compression for interface property extraction, J. Mater. Res. **33**, 424 (2018).

[24] J.-L. Huang and P. K. Nayak, in *Advances in Ceramic Matrix Composition*, edited by I. M. Low (Woodhead, Cambridge, UK, 2014), pp 218–234.

[25] I. Salehinia, S. Shao, J. Wang, and H. M. Zbib, Interface structure and the inception of plasticity in Nb/NbC nanolayered composites, Acta Mater. **86**, 331 (2015).

[26] M. R. Kayser and A. Adnan, Grain boundary driven mechanical properties of ZrB_2 and ZrC-ZrB_2 nanocomposite: A molecular simulation study, J. Am. Ceram. Soc. **101**, 3105 (2018).

[27] Y. M. An, X. H. Zhang, W. B. Han, P. Hu, G. Q. Chen, and G. D. Zhao, Interface of graphene/ZrB_2 ceramics structure by molecular dynamics simulation, Key Eng. Mater. **655**, 82 (2015).

[28] R. Shahsavari, Intercalated hexagonal boron nitride/silicates as bilayer multifunctional ceramics, ACS Appl. Mater. Interfaces **10**, 2203 (2018).

[29] L. Shi, A. Xu, and T. Zhao, First-principles investigations of the working mechanism of 2D h-BN as an interfacial layer for the anode of lithium metal batteries, ACS Appl. Mater. Interfaces **9**, 1987 (2017).

[30] Y. Zhu, X. He, and Y. Mo, Origin of outstanding stability in the lithium solid electrolyte materials: insights from thermodynamic analyses based on first-principles calculations, ACS Appl. Mater. Interfaces **7**, 23685 (2015).

[31] P. E. Blöchl, Projector augmented-wave method, Phys. Rev. B **50**, 17953 (1994).

[32] G. Kresse and D. Joubert, From ultrasoft pseudopotentials to the projector augmented-wave method, Phys. Rev. B **59**, 1758 (1999).

[33] J. P. Perdew, K. Burke, and M. Ernzerhof, Generalized Gradient Approximation Made Simple, Phys. Rev. Lett. **77**, 3865 (1996).

[34] S. Grimme, Semiempirical GGA-type density functional constructed with a long-range dispersion correction, J. Comput. Chem. **27**, 1787 (2006).

[35] Y. Zhang and S. Sanvito, First-principles investigation of the thermodynamic stability of MB_2 materials surfaces ($M = $ Ti/Zr/Hf), J. Am. Ceram. Soc. **101**, 4118 (2018).

[36] X. Chen, F. Tian, C. Persson, W. Duan, and N. Chen, Interlayer interactions in graphites, Sci. Rep. **3**, 3046 (2013).

[37] L. Tengdelius, J. Lu, U. Forsberg, X. Li, L. Hultman, E. Janzén, and H. Högberg, ZrB_2 thin films deposited on GaN(0001) by magnetron sputtering from a ZrB_2 target, J. Cryst. Growth **453**, 71 (2016).

[38] D. M. Stewart, D. J. Frankel, and R. J. Lad, Growth, structure, and high temperature stability of zirconium diboride thin films, J. Vac. Sci. Technol. A **33**, 31505 (2015).

[39] D. S. Koda, F. Bechstedt, M. Marques, and L. K. Teles, Coincidence lattices of 2D crystals: Heterostructure predictions and applications, J. Phys. Chem. C **120**, 10895 (2016).

[40] P. Paul, P. Chakraborty, T. Das, D. Nafday, and T. Saha-Dasgupta, Properties at the interface of graphene and Ti_2C MXene, Phys. Rev. B **96**, 035435 (2017).

[41] J. C. Meyer, A. K. Geim, M. I. Katsnelson, K. S. Novoselov, T. J. Booth, and S. Roth, The structure of suspended graphene sheets, Nature (London) **446**, 60 (2007).

[42] G. Giovannetti, P. A. Khomyakov, G. Brocks, V. M. Karpan, J. V. D. Brink, and P. J. Kelly, Doping Graphene with Metal Contacts, Phys. Rev. Lett. **101**, 026803 (2008).

[43] Y. Jiang, Y. Wei, J. R. Smith, J. W. Hutchinson, and A. G. Evans, First principles based predictions of the toughness of a metal/oxide interface, Int. J. Mater. Res. **101**, 8 (2010).

[44] P. Lazar and R. Podloucky, Cleavage fracture of a crystal: Density functional theory calculations based on a model which includes structural relaxations, Phys. Rev. B **78**, 104114 (2008).

[45] M. Kanani, A. Hartmaier, and R. Janisch, Interface properties in lamellar TiAl microstructures from density functional theory, Intermetallics **54**, 154 (2014).

[46] G. Henkelman, B. P. Uberuaga, and H. Jonsson, A climbing image nudged elastic band method for finding saddle points and minimum energy paths, J. Chem. Phys. **113**, 9901 (2000).

[47] G. Henkelman and H. Jonsson, Improved tangent estimate in the nudged elastic band method for finding minimum energy paths and saddle points, J. Chem. Phys. **113**, 9978 (2000).

[48] T. Csanádi, A. Kovalčíková, J. Dusza, W. G. Fahrenholtz, and G. E. Hilmas, Slip activation controlled nanohardness anisotropy of ZrB_2 ceramic grains, Acta Mater. **140**, 452 (2017).

[49] H. Xiong, Z. Liu, H. Zhang, Z. Du, and C. Chen, First principles calculation of interfacial stability, energy and electronic properties of SiC/ZrB_2 interface, J. Phys. Chem. Solids **107**, 162 (2017).

[50] B.-T. Wang, W. Zhang, and W.-D. Li, Mechanics, lattice dynamics, and chemical bonding in ZrB_2 and ZrB_{12} from first-principles calculations, Sci. Adv. Mater. **5**, 1916 (2013).

[51] T. A. Manz and N. G. Limas, Introducing DDEC6 atomic population analysis: Part 1. Charge partitioning theory and methodology, RSC Adv. **6**, 47771 (2016).

[52] N. G. Limas and T. A. Manz, Introducing DDEC6 atomic population analysis: Part 2. Computed results for a wide range of periodic and nonperiodic materials, RSC Adv. **6**, 45727 (2016).

[53] T. A. Manz, Introducing DDEC6 atomic population analysis: Part 3. Comprehensive method to compute bond orders, RSC Adv. **7**, 45552 (2017).

[54] A. J. Neel, M. J. Hilton, M. S. Sigman, and F. D. Toste, Exploiting non-covalent π interactions for catalyst design, Nature (London) **543**, 637 (2017).

[55] P. Miranzo, M. Belmonte, and M. I. Osendi, From bulk to cellular structures: A review on ceramic/graphene filler composites, J. Eur. Ceram. Soc. **37**, 3649 (2017).

[56] X. Zhang, C. Shi, E. Liu, N. Zhao, and C. He, Effect of interface structure on the mechanical properties of graphene nanosheets reinforced copper matrix composites, ACS Appl. Mater. Interfaces **10**, 37586 (2018).